Critical speed for capillary-gravity surface flows in the dispersive shallow water limit

Chi-Tuong Pham[a)]
Laboratoire de Physique Statistique de l'Ecole Normale Supérieure, associé au CNRS et aux Universités Paris VI et VII, 24 Rue Lhomond, 75231 Paris, France

Caroline Nore[b)]
Département de Physique, Université Paris XI, 91405 Orsay Cedex, France and Laboratoire d'Informatique pour la Mécanique et les Sciences de l'Ingénieur, CNRS, Boîte Postale 133, 91403 Orsay Cedex, France

Marc-Étienne Brachet[c)]
Laboratoire de Physique Statistique de l'Ecole Normale Supérieure, associé au CNRS et aux Universités Paris VI et VII, 24 Rue Lhomond, 75231 Paris, France

(Received 12 October 2004; accepted 14 March 2005; published online 31 May 2005)

The stability of perfect-fluid capillary-gravity surface flows past a cylindrical obstacle is studied in the shallow water limit, using the two-dimensional compressible Euler equations, with leading-order dispersive corrections. Stationary solutions with different contact angles are obtained by Newton branch following, based on Fourier pseudospectral methods, using mapped Chebychev polynomials. Stable and unstable branches are found to meet, through a saddle-node bifurcation, at a critical speed beyond which no stationary solution exists. For large obstacles, the stable branch is compared with the stationary solutions of the compressible Euler equation without dispersion. Boundary layers are investigated. In this regime, the unstable dynamics are shown to lead to a finite-time dewetting singularity. © *2005 American Institute of Physics*. [DOI: 10.1063/1.1926267]

I. INTRODUCTION

Nonlinear problems involving capillary and gravity effects in free surface perfect flows, such as the generation and radiation of capillary-gravity waves by a moving obstacle, have attracted much attention.[1,2]

Although the existence of a critical speed for the onset of capillary-gravity wave drag is well established, there remains a controversy on the order of the transition. In the infinite depth limit, early theoretical work[3] and experiments[4] were in favor of a discontinuous (or first-order) transition. However, another experimental result published at the same time[5] favored a continuous (or second-order) transition. It was suggested in this paper and in the following extended paper[6] that the large scatter observed in the former experiment[4] was the result of uncontrolled pinning and stick slip due to wetting and capillary forces that considerably exceed the wave drag. It was also argued that this scatter was interpreted by the authors of the former experiment as a discontinuous transition. Moreover, by switching on and off the feedback, Burghelea and Steinberg[5] showed the crucial role of capillary forces in altering the results of measurements of the wave drag force. It thus appears that experimentally only continuous transition to the wave drag state was observed.

Later on, it was suggested[7] that two different results on the order of the transition could be obtained, depending on the experimental condition: at constant force on an immersed object a discontinuous transition should be observed, while at constant depth of an immersed object a continuous transition should be found. However, this qualitative agreement with the experiment was not entirely satisfactory, since the predicted transition was rather sharp and very different functionally from the experimental one. Furthermore, the behavior of the wave drag above the transition was not in a good agreement with the experimental observations.

On balance, it thus appears crucial not to neglect the wetting and capillary forces on the immersed object. As a first step in this direction we will study here the shallow water limit where the problem becomes quasi-two-dimensional.

When the channel depth is infinite, it was recognized[5,6] that, due to the existence of a wave number at which the phase speed is minimum, the problem has a deep analogy with that of the breakdown of superfluidity in a model of helium[8] that includes roton excitations.

At finite depth, it is well known that two distinct regimes exist for the propagation of linear waves. If the depth is large enough, a regime analogous to the infinite depth one is obtained with a negative dispersive term. In contrast, if the depth is small enough, the dispersion changes sign and there is no minimum in phase speed.

The present study is devoted to that latter small-depth regime. This regime is analogous to the problem of breakdown of superfluidity when only phonon excitations are present.[9–11] It also corresponds to the experimentally observed critical speed for onset of dissipation in Bose–Einstein condensates.[12]

The paper is organized as follows. In Sec. II we show that the small-depth regime can be studied in the shallow

[a)]Electronic mail: pham@lps.ens.fr
[b)]Electronic mail: nore@limsi.fr
[c)]Electronic mail: brachet@lps.ens.fr

water limit where the problem becomes two dimensional. Section III is devoted to the derivation of the boundary layer analytical expressions for Neumann boundary conditions; Sec. IV contains validations of the numerical procedure and new results on bifurcation diagrams and critical Mach numbers; in Sec. V, our results on the dynamical regime are reported, paying particular attention to a finite-time dewetting singularity; finally Sec. VI is our conclusion. The specially adapted numerical method used in this work is detailed in the Appendix.

II. PRESENTATION OF THE MODEL

In this section, we present the approximated two-dimensional equations that model the effect of a disk of radius unity (diameter $D=2$), moving at constant speed $\mathbf{v}=v\mathbf{e}_x$ in a shallow layer fluid at rest.

We first discuss this approximation in term of waves propagating on a fluid layer and then introduce the cylindrical obstacle. We next propose a variational formulation associated with our dispersive shallow water equations (DSWE). We introduce also a relaxation procedure allowing to reach steady solutions in a simple manner.

A. Dispersion relation with surface tension

Let us first consider waves propagating on a fluid layer with no obstacle. Specifically, we are interested in the dynamics of surface disturbances of vertical amplitude a and typical horizontal length scale k^{-1}, in a fluid of depth H and surface tension σ.

In the linear regime, $a/H \ll 1$ and $ka \ll 1$, the dispersion relation reads[2]

$$\omega^2(k) = k\left(g + \frac{k^2\sigma}{\mu}\right)\tanh(Hk), \tag{1}$$

where μ is the fluid density and g the gravity acceleration.

In the infinite depth limit $H \to \infty$, the dispersion relation reads

$$\omega^2(k) = \frac{gk(2 + k^2\ell_c^2)}{2}, \tag{2}$$

where $\ell_c = \sqrt{2\sigma/g\mu}$ is the capillary length.[1] In this limit, the phase speed $c_\varphi(k) = \omega(k)/k$ admits a local minimum $c_m = 2^{1/4}\sqrt{g\ell_c}$ at wave number $k_m = \sqrt{2}/\ell_c$.

For finite depth H, the dispersion relation (1) can be expressed in terms of the gravity wave speed $c = \sqrt{gH}$ as

$$\omega^2(k) = \frac{c^2k(2 + k^2\ell_c^2)\tanh(Hk)}{2H}. \tag{3}$$

Two different regimes can be distinguished.

The large-depth regime, $H > \sqrt{3/2}\ell_c$, is similar to the infinite depth regime. The phase speed $c_\varphi(k)$ admits a minimum at a finite wave number k_m (see Fig. 1), related to the capillary length ℓ_c by

$$\ell_c = \frac{\sqrt{2}}{k_m}\sqrt{1 - \frac{4Hk_m}{2Hk_m + \sinh(2Hk_m)}}. \tag{4}$$

The minimum phase speed $c_m < c$ is related to k_m by

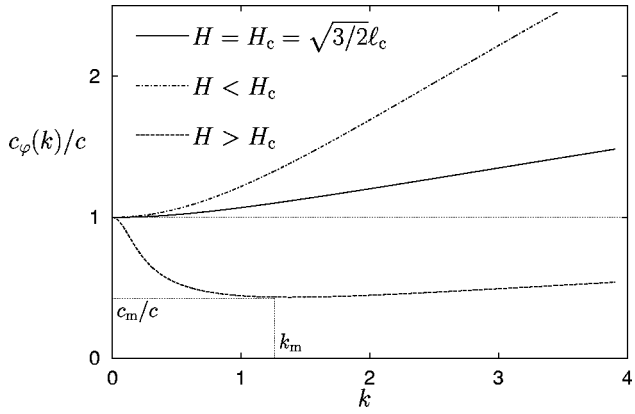

FIG. 1. Nondimensionalized phase speed $c_\varphi(k) = \omega(k)/ck$ [see Eq. (1)], where $c = \sqrt{gH}$ is the gravity wave speed. In the large-depth regime ($H > H_c$), the curve displays a minimum similar to the roton minimum in superfluid, whereas in the small-depth regime ($H < H_c$), the minimum phase velocity is that of the gravity waves c at $k=0$. The small-depth regime is the regime studied in this paper.

$$c_m = 2c\sqrt{\frac{\sinh(Hk_m)^2}{Hk_m[2Hk_m + \sinh(2Hk_m)]}}. \tag{5}$$

Note that this minimum is somewhat equivalent to the roton minimum in the dispersion relation of superfluid helium.[1,8]

Conversely, in the small-depth regime, $H < \sqrt{3/2}\ell_c$, the phase velocity is a strictly increasing function of k (see Fig. 1). Taylor expanding $\omega^2(k)$ around $k=0$ yields

$$\omega^2(k) = c^2\left[k^2 + k^4\left(\frac{\ell_c^2}{2} - \frac{H^2}{3}\right)\right], \tag{6}$$

showing that dispersion effects are controlled by an effective capillary length defined by

$$\xi = \sqrt{\ell_c^2 - \tfrac{2}{3}H^2}. \tag{7}$$

Note that in this regime, the dispersion relation (6) is similar to that encountered in the Gross–Pitaevskii equation, also called the nonlinear Schrödinger equation (NLS), modeling superfluids[1,13,14] or accurately describing Bose–Einstein condensates.[15]

In the following, the fluid layer is supposed to be smaller than $\sqrt{3/2}\ell_c$ and the fluid is considered as inviscid. Note that this supposes that although the flow is thin, viscous effects are small enough to be neglected.

Let us be more quantitative on this aspect of the problem. At leading order, we can estimate the viscous effects within two different approximations: for very thin films in the lubrication approximation and for thicker films in the boundary layer approximation. On the one hand, the lubrication approximation[16] gives the damping time scale $\tau_l = H^2/\nu$, where ν is the fluid kinematic viscosity. Viscous effects can be neglected if τ_l is greater than the time scale of advection $\tau_a = D/U$, where U is of the order of gravity wave speed c. On the other hand, the boundary layer approximation gives the following thickness of the boundary layer $\delta = D/\sqrt{\mathrm{Re}}$, with $\mathrm{Re} = UD/\nu$. Viscous effects are negligible if $\delta \ll \xi$ which amounts to $\nu/\xi U \ll \xi/D$. For a water layer of thickness $H \simeq 1$ mm and viscosity $\nu \simeq 10^{-6}$ m^2 s^{-1}, we find $\tau_l \simeq 1$ s and

$\tau_a \simeq D/c$. Thus viscous effects are small provided that $D < 0.1$ m. Turning now to boundary layer effects, the condition for viscous effects to be small yields $\xi/D \gg 3\times 10^{-3}$. Therefore, there is a range of diameter 1 mm $< D <$ 10 cm for which the viscosity can be neglected in the regimes we study.

The model we study is formally very close to the NLS equation describing superflows, the capillary length ξ playing the role of the so-called coherence length. It is thus of interest to compare both systems. Moreover, the model of an inviscid flow past an obstacle in the small-depth regime (i.e., with no local minimum for the phase velocity) has not yet been studied.

B. Two-dimensional reduction

Taking into account nonlinear effects and dominant order dispersive effects, in the small-depth linear regime, our shallow water approximation[2] reads, in the frame of a cylindrical obstacle of unit radius, moving at speed $\mathbf{v} = +v\mathbf{e}_x$,

$$\partial_t \phi = \tfrac{1}{2}c^2\xi^2\Delta\rho - \tfrac{1}{2}(\boldsymbol{\nabla}\phi)^2 + c^2(1-\rho) + \mathbf{v}\cdot\boldsymbol{\nabla}\phi, \tag{8}$$

$$\partial_t \rho = -\rho\Delta\phi - \boldsymbol{\nabla}\rho\cdot\boldsymbol{\nabla}\phi + \mathbf{v}\cdot\boldsymbol{\nabla}\rho, \tag{9}$$

where ρ stands for the thickness of the fluid layer (nondimensionalized by H), ϕ is the horizontal velocity potential, ξ is the effective capillary length renormalized by the effects of finite depth given by Eq. (7), and c the gravity wave speed. Note that the standard shallow water equation does not contain the dispersive correction.

Defining the velocity in the obstacle frame as

$$\mathbf{U} = \boldsymbol{\nabla}\phi - \mathbf{v}, \tag{10}$$

Eq. (9) reads

$$\partial_t \rho + \boldsymbol{\nabla}\cdot(\rho\mathbf{U}) = 0. \tag{11}$$

Therefore, the system (8) and (11) yields, respectively, to the Bernoulli equation (with a supplementary dispersive term depending on ξ) and the continuity equation for a barotropic compressible and irrotational flow. These equations are our DSWE in the presence of a disk.

The boundary conditions on the obstacle $r=1$ read

$$\partial_r \rho = \cot\alpha_0/H = \rho_0', \tag{12}$$

$$\partial_r(\phi - \mathbf{v}\cdot\mathbf{r}) = 0, \tag{13}$$

the angle α_0 being the contact angle of the liquid on the obstacle measured with respect to the ascendant vertical (see Fig. 2). For convenience, we denote $\rho_0' = \cot\alpha_0/H$, the derivative of ρ with respect to r at the cylinder which has the dimension of the inverse of a length. The Neumann boundary condition (12) physically corresponds to a hydrophobic obstacle for $\alpha_0 \in [0:\pi/2[$ or $\rho_0' > 0$ and to a hydrophilic obstacle for $\alpha_0 \in]\pi/2:\pi]$ or $\rho_0' < 0$. The particular value $\alpha_0 = \pi/2$ corresponds to a homogeneous Neumann condition $\rho_0' = 0$.

Note that, for $\xi = 0$, Eqs. (8) and (9) reduce to the Euler equations for a compressible barotropic fluid, with Eq. (13) as the unique boundary condition. The stationary solutions of the two-dimensional Eulerian flow and the critical Mach number have been calculated previously.[17]

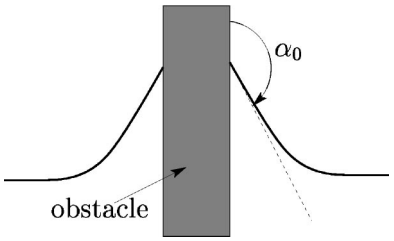

FIG. 2. Definition of the contact angle α_0 at the cylinder. It corresponds to the Neumann boundary condition $\partial_r\rho|_{\partial\Omega} = \cot\alpha_0/H = \rho_0'$ [Eq. (12)].

We denote by Ω the plane $\mathbb{C}$ deprived of $\mathbb{D}$ the disk of radius unity and by $\partial\Omega$ the boundary of the domain, that is, the circle of radius unity. We will naturally use the polar coordinates (r,θ) such that $x = r\cos\theta$ and $y = r\sin\theta$, and the associated unit vectors are denoted by $(\mathbf{e}_r, \mathbf{e}_\theta)$.

C. Variational formulation

In the rest of the paper, we use $c^2 = 1$.

The dispersive shallow water equations may be derived from the following action functional (with $\mathbf{n} = -\mathbf{e}_r$ the unitary external normal):

$$\mathcal{E} = \int_\Omega d^2x\left[\frac{1}{2}\rho(\boldsymbol{\nabla}\phi)^2 + \frac{1}{2}(\rho-1)^2 + \frac{1}{2}\xi^2(\nabla\rho)^2\right] - \frac{1}{2}\xi^2\oint_{\partial\Omega} d\ell\,\mathbf{n}\rho\,\boldsymbol{\nabla}\rho, \tag{14}$$

$$\mathcal{P} = \int_\Omega d^2x[(\rho-1)\,\boldsymbol{\nabla}\phi] + \oint_{\partial\Omega} d\ell\,\mathbf{n}\phi, \tag{15}$$

$$\mathcal{F} = \mathcal{E} - \mathbf{v}\cdot\mathcal{P}, \tag{16}$$

$$\mathcal{A} = -\int dt\{\rho\partial_t\phi + \mathcal{F}\}, \tag{17}$$

by considering the Euler–Lagrange $\delta\mathcal{A}/\delta\rho = 0$ and $\delta\mathcal{A}/\delta\phi = 0$ associated to (17). Note the presence of supplementary boundary terms on $\partial\Omega$ that ensure the appropriate boundary conditions on the obstacle.

This formulation stresses that the dynamics under the DSWE is conservative. Therefore, in order to obtain stationary solutions from arbitrary initial conditions, we need to proceed through a relaxation procedure.

D. Relaxation toward steady states

Our aim is to find steady solutions starting from arbitrary initial conditions. Note that the equations

$$\partial_t\rho = \tfrac{1}{2}\xi^2\Delta\rho - \tfrac{1}{2}(\boldsymbol{\nabla}\phi)^2 + 1 - \rho + \mathbf{v}\cdot\boldsymbol{\nabla}\phi, \tag{18}$$

$$\partial_t \phi = \rho \Delta \phi + \nabla \rho \cdot \nabla \phi - \mathbf{v} \cdot \nabla \rho, \tag{19}$$

admit the same stationary solutions than Eqs. (8) and (9) (with $c^2=1$). However, this relaxation method can only reach stable stationary solutions. In order to also capture unstable stationary solutions,[18] we apply to Eqs. (18) and (19) the Newton branch-following method that is detailed in the Appendix.

III. BOUNDARY LAYER SOLUTIONS: ANALYTICAL RESULTS

We now present calculations of the stationary solutions in the limit $\xi/\sqrt{2}D \to 0$. For nonzero Mach number

$$\mathcal{M} = |\mathbf{v}|/c = |\mathbf{v}|, \tag{20}$$

we define the new phase variable[19]

$$\varphi = -(\phi - vr\cos\theta)/v. \tag{21}$$

The Bernoulli (8) and continuity (9) equations then read

$$0 = \frac{1}{2}\xi^2 \Delta\rho - \rho + 1 + \frac{\mathcal{M}^2}{2}[1 - (\nabla\varphi)^2], \tag{22}$$

$$0 = \rho\Delta\varphi + \nabla\rho\cdot\nabla\varphi. \tag{23}$$

The boundary conditions now read

$$\partial_r \rho|_{\partial\Omega} = \rho_0',$$

$$\partial_r \varphi|_{\partial\Omega} = 0.$$

At finite but small Mach number, we expand ρ and φ as

$$\rho = \rho^{\langle 0\rangle} + \mathcal{M}^2\rho^{\langle 1\rangle} + \cdots + \mathcal{M}^{2k}\rho^{\langle k\rangle} + \cdots, \tag{24}$$

$$\varphi = \varphi^{\langle 0\rangle} + \mathcal{M}^2\varphi^{\langle 1\rangle} + \cdots + \mathcal{M}^{2k}\varphi^{\langle k\rangle} + \cdots. \tag{25}$$

Note that if one knows φ at order $\mathcal{M}^{2k}$, one can formally deduce ρ at order $\mathcal{M}^{2(k+1)}$ by solving (22). The potential φ can then be computed at order $\mathcal{M}^{2(k+1)}$ by solving (23). In order to compute φ, we will have to solve equations of the type

$$\frac{d^2y}{dr^2}(r) + \frac{1}{r}\frac{dy}{dr}(r) - \frac{n^2}{r^2}y(r) = \mathrm{RHS}(r), \tag{26}$$

where RHS is the right-hand side.

Solutions to the corresponding homogeneous equation are

$$y(r) = Ar^n + Br^{-n}, \tag{27}$$

so that the general equation with nonzero RHS(r) can be computed using the method of variation of parameter. Using the boundary conditions $\lim_{r\to+\infty} y(r)=0$ and $dy/dr(r=1)=0$ yields for the solution of the inhomogeneous equation the explicit expression

$$y(r) = -\frac{r^{-n}}{2}\int_1^{+\infty} \mathrm{RHS}(u)(u^{1+n} + u^{1-n})du - \frac{r^n}{2}\int_r^{+\infty} u^{1-n}\mathrm{RHS}(u)du + \frac{r^{-n}}{2}\int_r^{+\infty} u^{n+1}\mathrm{RHS}(u)du, \tag{28}$$

provided that the function RHS decreases rapidly enough at infinity. Note that the first term of $y(r)$ leads to a term of the type C/r. Due to the expressions of RHS encountered in the following computations, the two last terms will turn out to tend to zero exponentially (on a length scale of order ξ), so that the behavior at infinity of the function y will be governed by a long-range algebraic term that reads

$$y(r) \underset{r\to+\infty}{\sim} -\frac{1}{2r^n}\int_1^{+\infty} \mathrm{RHS}(u)(u^{1+n} + u^{1-n})du. \tag{29}$$

A. Case of inhomogeneous Neumann conditions ($\rho_0' \neq 0$)

We now turn to the computation of the stationary solution in the general case of inhomogeneous Neumann boundary conditions $\rho_0' \neq 0$. Expressions for $\rho^{\langle 0\rangle}$ and $\varphi^{\langle 0\rangle}$ are obviously needed to bootstrap the iteration. When the Mach number is zero, $\varphi=0$ is solution of the stationary equations and ρ satisfies

$$\tfrac{1}{2}\xi^2\Delta\rho^{\langle 0\rangle} - \rho^{\langle 0\rangle} + 1 = 0. \tag{30}$$

The solution of this equation with the correct boundary conditions reads

$$\rho^{\langle 0\rangle} = 1 - \frac{\rho_0'\xi}{\sqrt{2}} K_0\left(\frac{\sqrt{2}r}{\xi}\right) \Big/ K_1\left(\frac{\sqrt{2}}{\xi}\right), \tag{31}$$

where K_n is the (order n) modified Bessel function. The profile $\rho^{\langle 0\rangle}-1$ is displayed in Fig. 3(a).

The velocity potential $\varphi^{\langle 0\rangle}$ then satisfies

$$\Delta\varphi^{\langle 0\rangle} = -\nabla\rho^{\langle 0\rangle}\cdot\nabla\varphi^{\langle 0\rangle} + (1-\rho^{\langle 0\rangle})\Delta\varphi^{\langle 0\rangle}. \tag{32}$$

We write

$$\varphi^{\langle 0\rangle} = \varphi^{\langle 0\rangle}_{\mathrm{Euler}} + \tilde{\varphi}^{\langle 0\rangle}, \tag{33}$$

where $\varphi^{\langle 0\rangle}_{\mathrm{Euler}} = (r+1/r)\cos\theta$ is the solution at order 0 in $\mathcal{M}^2$ of the Eulerian flow. Using the relation $\Delta\varphi^{\langle 0\rangle}_{\mathrm{Euler}}=0$, Eq. (32) yields the following equation for $\tilde{\varphi}^{\langle 0\rangle}$:

$$\Delta\tilde{\varphi}^{\langle 0\rangle} = -\nabla\rho^{\langle 0\rangle}\cdot\nabla\varphi^{\langle 0\rangle}_{\mathrm{Euler}} - \nabla\rho^{\langle 0\rangle}\cdot\nabla\tilde{\varphi}^{\langle 0\rangle} + (1-\rho^{\langle 0\rangle})\Delta\tilde{\varphi}^{\langle 0\rangle}. \tag{34}$$

This equation cannot be solved directly. We keep in the right-hand side, at the dominant order of the computations, the first term and drop the two others. The function $\tilde{\varphi}^{\langle 0\rangle}$ is then the solution of the equation

$$\Delta\tilde{\varphi}^{\langle 0\rangle} = -\nabla\rho_0^{\langle 0\rangle}\cdot\nabla\varphi^{\langle 0\rangle}_{\mathrm{Euler}}. \tag{35}$$

The expression of $\tilde{\varphi}^{\langle 0\rangle}$ can be computed using Eq. (28). The potential $\varphi^{\langle 0\rangle}$ (33) is shown in Fig. 3(b) computed with

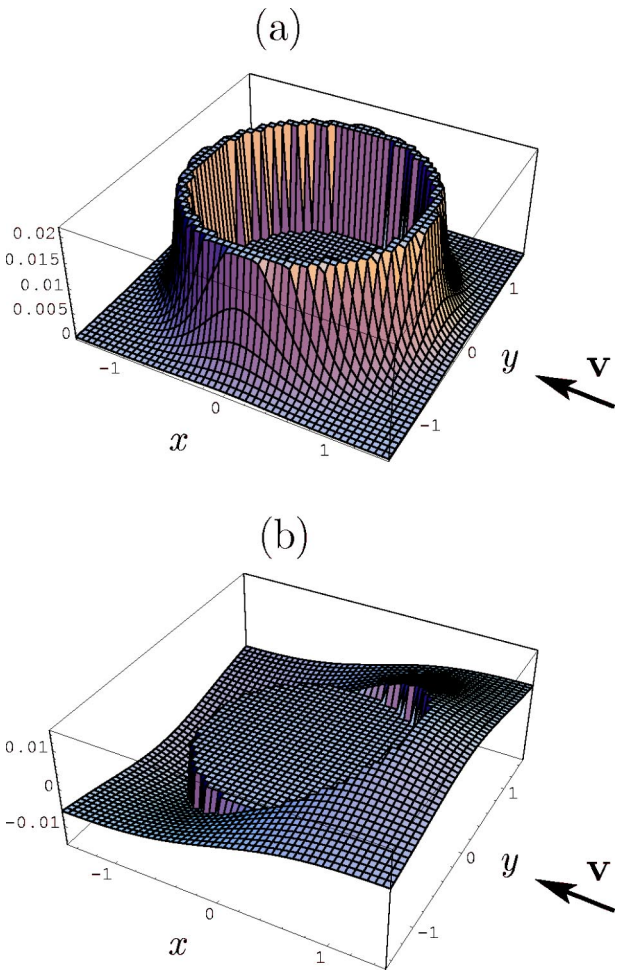

FIG. 3. (Color online). Plots of (a) $\rho^{\langle 0\rangle}-1$ [Eq. (31)] and (b) $\varphi^{\langle 0\rangle}$ [Eq. (33)] for $\xi/\sqrt{2}D=1/20$ and $\rho_0'=-1$.

MATHEMATICA. Equation (29) yields, far from the obstacle and in the limit $\xi/\sqrt{2}D\to 0$,

$$\tilde{\varphi}^{\langle 0\rangle} \underset{r\to+\infty}{\sim} \frac{\rho_0'\xi^2}{r}\cos\theta. \tag{36}$$

Note that the compressible Eulerian flow around a disk of radius r_1 admits at order zero in $\mathcal{M}^2$ the following solution:

$$\varphi^{\langle 0\rangle}_{\mathrm{Euler},r_1} = \left(r+\frac{r_1^2}{r}\right)\cos\theta, \tag{37}$$

in order to satisfy the boundary condition $\partial_r\varphi^{\langle 0\rangle}_{\mathrm{Euler},r_1}=0$. Thus, the correction in $\varphi^{\langle 0\rangle}$ to $\varphi^{\langle 0\rangle}_{\mathrm{Euler}}$ is a long-range term that can be physically interpreted as a renormalization of the diameter of the disk: at large distances the flow is equivalent to an Eulerian flow around a disk of radius r_{eff} given by

$$\left(\frac{r_{\mathrm{eff}}}{r_0}\right)^2 = 1+\frac{\rho_0'\xi^2}{r_0}+O(\xi^3). \tag{38}$$

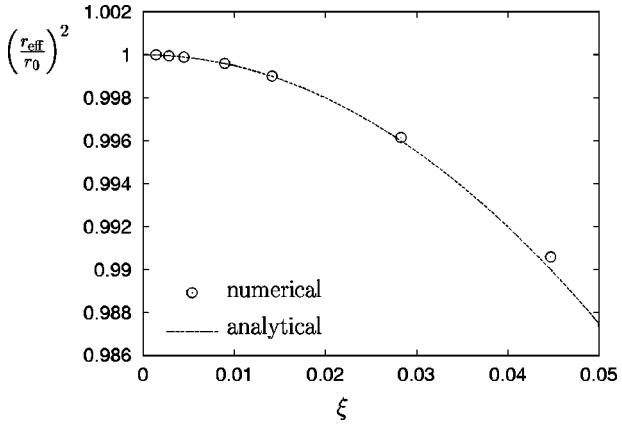

FIG. 4. Plot of the analytical renormalized radius [dashed line, see Eq. (38)] as a function of ξ together with the numerical solutions (dots). The contact angle on the cylinder perimeter is such that $\rho_0'=-5$, and the Mach number is $\mathcal{M}=0.001$. The agreement is very good for small $\xi/\sqrt{2}D$.

B. Case of homogeneous Neumann condition ($\rho_0'=0$)

The same procedure with homogeneous Neumann boundary condition $\rho_0'=0$ can be shown to lead to a renormalized radius[17]

$$\left(\frac{r_{\mathrm{eff}}}{r_0}\right)^2 = 1-\frac{3}{2}\mathcal{M}^2\left(\frac{\xi}{r_0}\right)^2. \tag{39}$$

Note that contrary to the case $\rho_0'\neq 0$, this effective size depends on the Mach number.

IV. STATIONARY SOLUTIONS

This section is devoted to the numerical determination of stationary solutions using the branch-following method detailed in the Appendix. We first compare analytical results of Sec. III with numerically obtained profiles of boundary layers with inhomogeneous Neumann conditions ($\rho_0'\neq 0$). It is a good test of the numerical precision and efficiency of our new method, which has already been checked in Ref. 17 in a superfluid context, with different equations of motion.

The rest of the section contains the numerical results on the bifurcation diagrams and the stationary solutions of the DSWE at small effective capillary lengths for the two types of Neumann boundary conditions: homogeneous and inhomogeneous. We study the dependence with the Mach number and the effective capillary length ξ of the solution profiles and show that unstable solutions far away on the branch can become unphysical by having negative density. We also study the dependence of the critical Mach number with ξ and with the contact angle.

A. Comparison with analytical boundary layer results for inhomogeneous Neumann conditions

We now compare the analytical results of Sec. III with numerically obtained solutions of boundary layers with inhomogeneous Neumann conditions. Figure 4 displays the analytical renormalized radius [Eq. (38)] as a function of ξ together with numerical results, obtained by computing the coefficient in $\cos\theta/r$ of the velocity potential of the station-

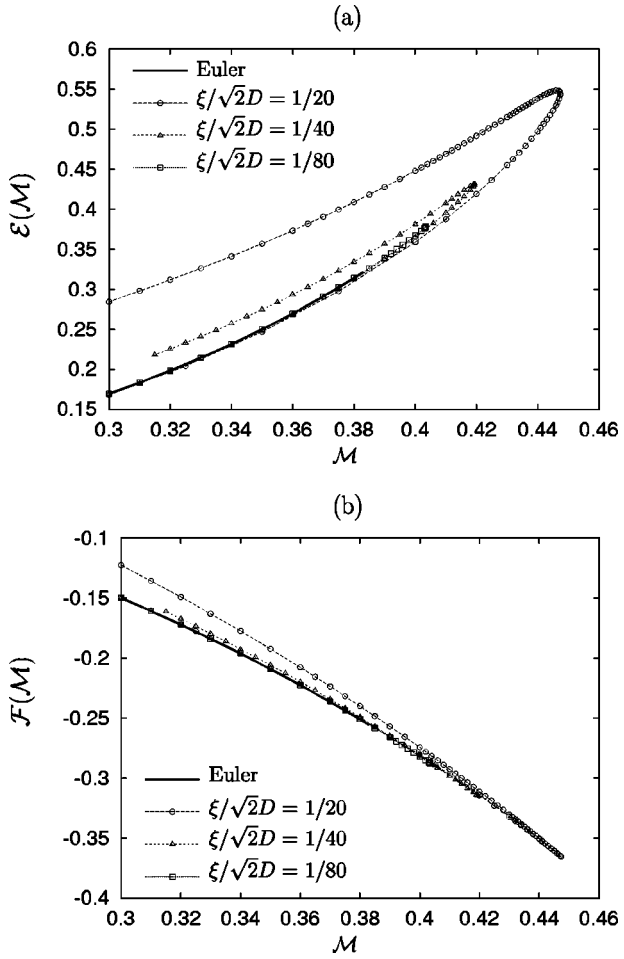

FIG. 5. Bifurcation diagrams for different $\xi/\sqrt{2}D$ and $\rho_0'=0$. The stable branch tends to the Euler branch when $\xi/\sqrt{2}D$ decreases. (a) Energy functional $\mathcal{E}$, (b) free energy functional $\mathcal{F}$.

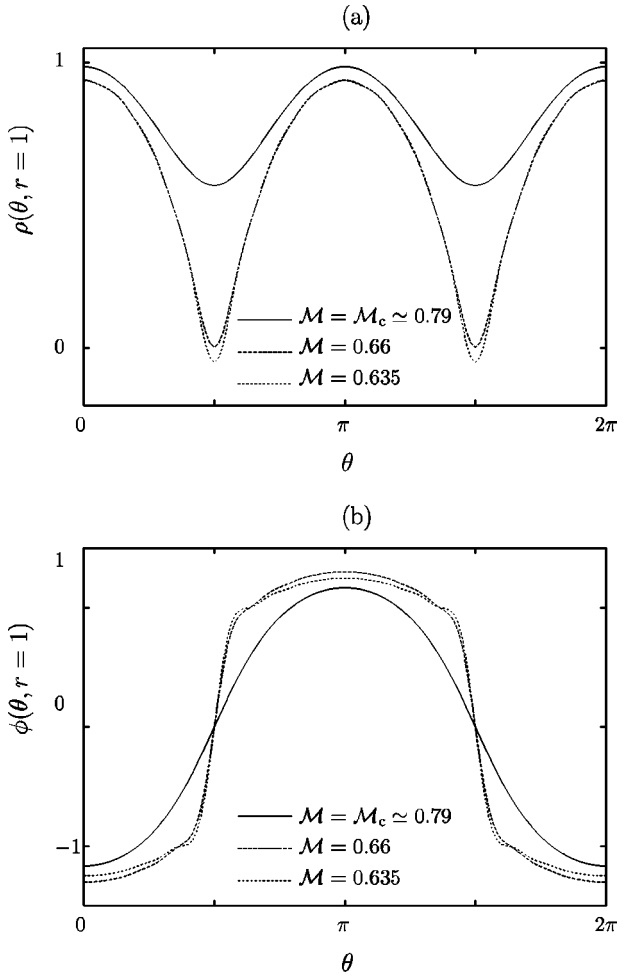

FIG. 6. Stationary solutions for $\xi/\sqrt{2}D=1/2$ and $\rho_0'=0$. (a) Density $\rho|_{\partial\Omega}$, (b) velocity potential $\phi|_{\partial\Omega}$. Note that the steady-state density can become negative for a certain Mach number far from $\mathcal{M}_c$. The phase varies continuously but is very steep when ρ is negative.

ary state. The agreement between analytical (dashed line) and numerical results (points) is very good for small $\xi/\sqrt{2}D$ emphasizing the ability of our method to compute thin boundary layers.

B. Bifurcation diagrams and stationary states

We present the bifurcation diagrams and the stationary solutions of the DSWE for the homogeneous Neumann boundary condition $\rho_0'=0$. The hydrophobic ($\rho_0'>0$) and hydrophilic ($\rho_0'<0$) cases lead to similar diagrams and solutions.

The values of $\mathcal{E}(\mathcal{M})-\mathcal{E}(0)$ and $\mathcal{F}(\mathcal{M})-\mathcal{F}(0)$ (the change of energies $\mathcal{E}$ and $\mathcal{F}$, relative to zero Mach number) are displayed in Fig. 5 as a function of the Mach number $\mathcal{M}$ for various values of $\xi/\sqrt{2}D$ and $\rho_0'=0$. As can be seen by the inspection of the figure, the stable stationary branches are almost superimposed on the Euler branch when $\xi/\sqrt{2}D$ decreases. For each $\xi/\sqrt{2}D$, the stable branch (lower branch) disappears with the unstable solution (upper branch) at a saddle-node bifurcation when $\mathcal{M}=\mathcal{M}_c$. There are no stationary solutions beyond this point. Furthermore, $\mathcal{F}(\mathcal{M})-\mathcal{F}(0)$ presents a cusp at the bifurcation point. This qualitative behavior is the signature of a Hamiltonian saddle-node bifurcation. This is the same type of bifurcation as that obtained in Bose–Einstein condensates.[11]

Density minima of the steady solutions are located on the disk border at $(\theta,r)=(\pm\pi/2,1)$ for $\rho_0'=0$. Unstable solu-

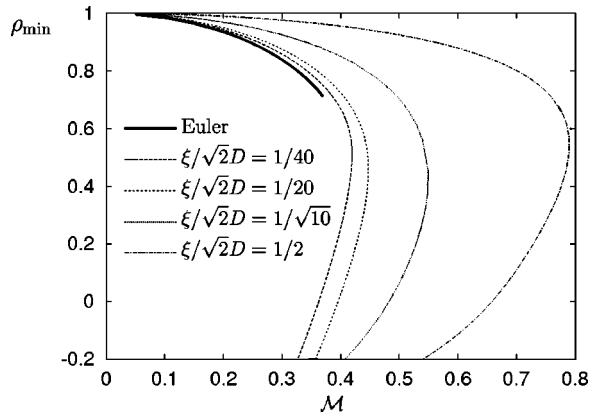

FIG. 7. Density minima $\rho_{\min}$ as a function of the Mach number $\mathcal{M}$ and the effective capillary length $\xi/\sqrt{2}D$ for $\rho_0'=0$. Note that, far enough on the unstable branch, the density can reach unphysical negative values for any ξ.

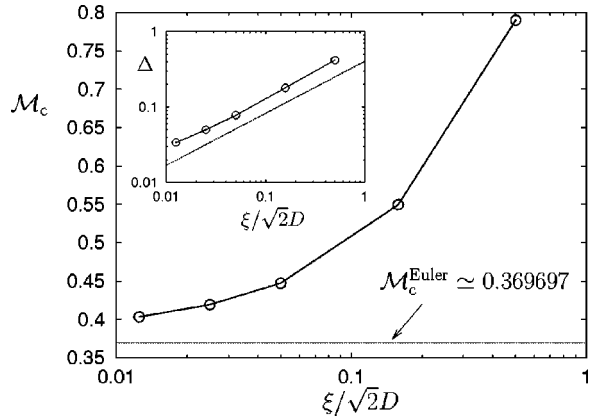

FIG. 8. Critical Mach number as a function of the effective capillary length for $\rho_0'=0$. Inset: difference Δ between the critical Mach number and the Eulerian one ($\Delta=\mathcal{M}_c-\mathcal{M}_c^{\text{Euler}}$) as a function of the effective capillary length for $\rho_0'=0$. It follows the scaling law $\Delta\sim(\xi/D)^\beta$ with $\beta\simeq 0.69$. The dashed line in the inset stands for $(\xi/D)^{0.69}$.

tions far from the bifurcation tip see their density decrease, reach zero, and become negative. A negative density solution is unphysical but is nevertheless solution of the DSWE. It can be inferred that it is dynamically unstable since the local sound speed satisfies

$$c_{\text{loc}}=\sqrt{gH\rho}, \tag{40}$$

the DSWE are thus unstable (because of the antipropagative instability) when $c_{\text{loc}}^2<0$.

Figure 6 shows that both the density and the phase go into the unphysical regime continuously. This behavior appears for any effective capillary length as shown in Fig. 7.

Figure 8 shows the variation of the critical Mach number with the effective capillary length: it increases with ξ and tends to the Euler value[17] $\mathcal{M}_c^{\text{Euler}}\simeq 0.369\,697\,052\,59(9)$ for $\xi/\sqrt{2}D\to 0$ following the scaling law $\mathcal{M}_c\simeq\mathcal{M}_c^{\text{Euler}}+\gamma(\xi/D)^\beta$ with $\beta\simeq 0.69$.

When $\rho_0'\neq 0$, the contact angle creates an exponentially decreasing boundary layer around the obstacle. Bifurcation diagrams similar to those found with $\rho_0'=0$ are obtained: stable and unstable branches meet at a saddle-node bifurcation, at a critical Mach number beyond which no stationary solution exists (data not shown). The only difference stems from the location of the density minima: for $\rho_0'>0$ (hydrophobic obstacle), the latter are located on the disk border while, for $\rho_0'<0$ (hydrophilic obstacle), they are situated at a finite distance from the disk (see Fig. 9).

Figure 10 reports the variation of the critical Mach number with the nature of the obstacle. The critical Mach number decreases linearly with ρ_0'.

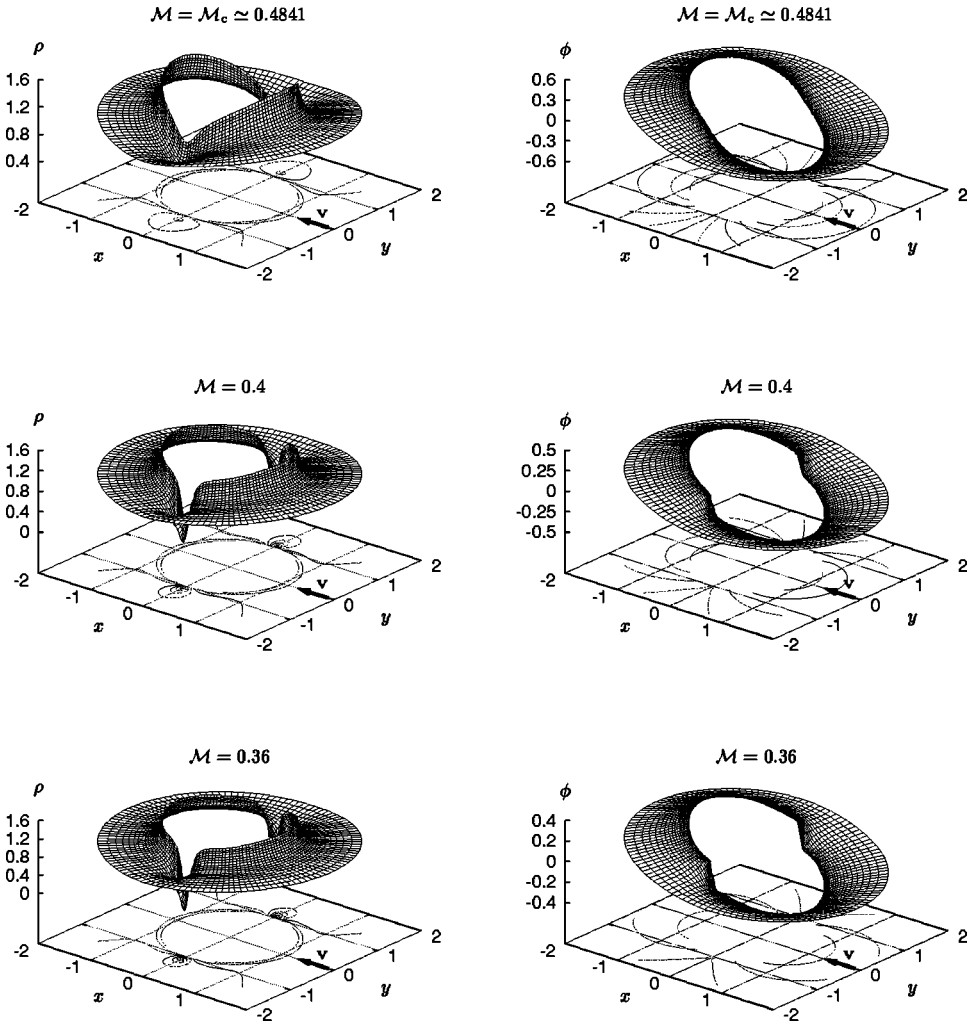

FIG. 9. Stationary density ρ (left) and velocity potential ϕ (right) for different Mach numbers. The density vanishes at finite distance of the obstacle in the case of a hydrophilic obstacle (here $\rho_0'=-5$ and $\xi/\sqrt{2}D=1/20$). From top to bottom: $\mathcal{M}=\mathcal{M}_c=0.4841$, 0.4 and 0.36. At critical Mach number, the free surface height is nonzero. The minimum of the density of the unstable solution gets closer to the cylinder and decreases far from the bifurcation. Its value eventually becomes unphysical (negative) (left bottom).

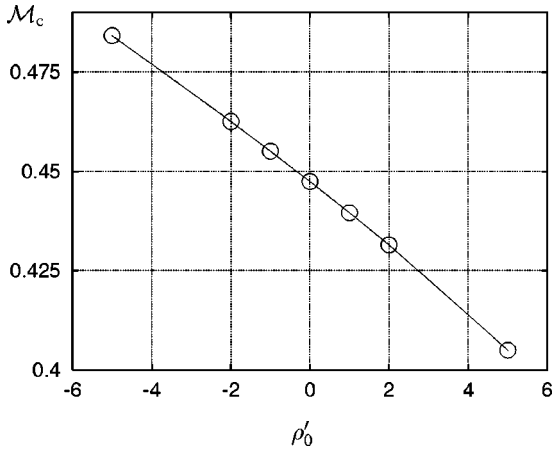

FIG. 10. Critical Mach number as a function of the Neumann boundary condition ρ_0' for $\xi/(\sqrt{2}D)=1/10$.

V. DYNAMICAL RESULTS: DEWETTING SINGULARITY

The stationary solutions obtained numerically provide us with adequate initial data for the study of dynamical solutions. Indeed, after a small perturbation, their integration in time will generate a dynamical evolution with emission of small amplitude capillary-gravity waves.

When perturbing an unstable steady solution, it relaxes toward the corresponding stable solution or it is destabilized. In this latter case, we always find that the density minima finally reach zero: the free surface of the fluid attains the layer bottom. This behavior appears to be a finite-time singularity that can be related to the dewetting singularity of a liquid on a hydrophobic solid. Such phenomenon is observed in falling fluid experiments.[20] A dry area is created, grows, and forms stationary arches.

In our case, the singularity is found to happen for any contact angle and takes place on the obstacle border for a hydrophobic disk as well as for the case $\rho_0'=0$ (see Fig. 11) or in the bulk for a hydrophilic obstacle (see Fig. 12). One can qualitatively study the nature of this finite-time singularity in the case $\rho_0'=0$. With this boundary condition, the density minimum located at $(\theta,r)=(\theta_{\min},1)$ is such that

$$\nabla\rho(\theta_{\min},1)=0. \tag{41}$$

Denoting $v_{\min}$ as the displacement velocity of this minimum, one can write

$$\frac{D\rho}{Dt}(\theta_{\min},1)=\frac{\partial\rho}{\partial t}(\theta_{\min},1)+\mathbf{v}_{\min}\cdot\nabla\rho(\theta_{\min},1) \tag{42}$$

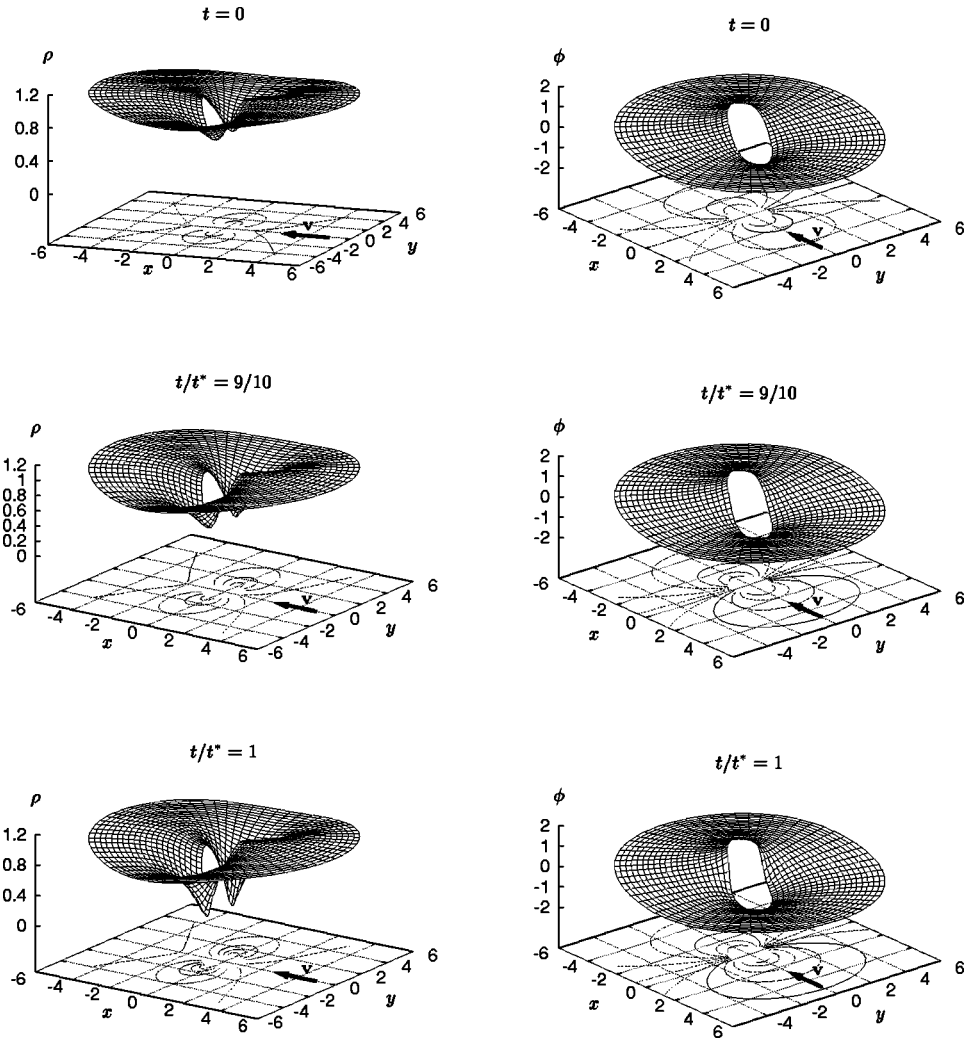

FIG. 11. Time evolution of the dewetting dynamics with $\rho_0'=0$ and $\xi/\sqrt{2}D=1/\sqrt{2}$ at time $t=0$, $t=(9/10)t^*$, $t=t^*$ where t^* is the singularity time. Left column, density ρ; right column, velocity potential ϕ. The velocity potential gets steeper like in a shock formation at t^*. The dewetting singularity (when ρ becomes negative) takes place on the obstacle border for $\rho_0'=0$.

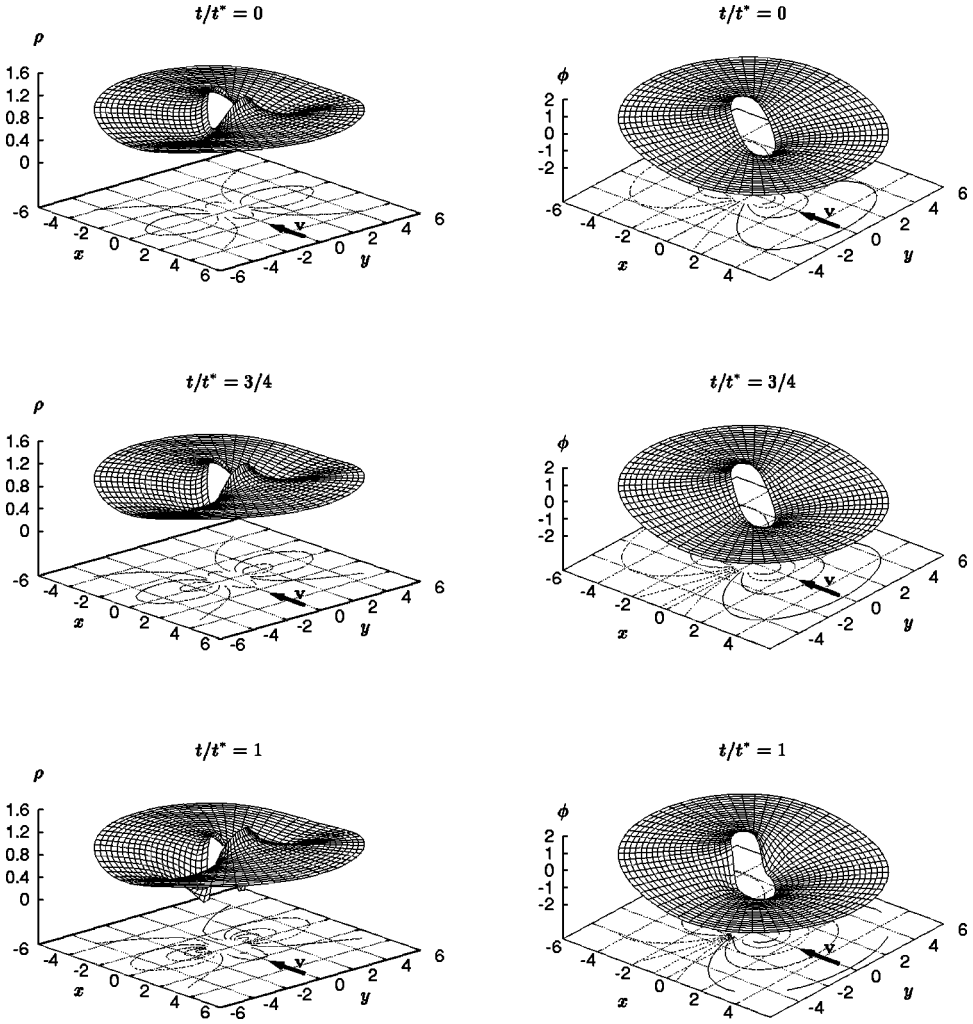

FIG. 12. Same as Fig. 11 (but at a distinct intermediate time) with $\rho_0'=-0.5$ (hydrophilic obstacle) and $\xi/\sqrt{2}D=1/\sqrt{2}$. The dewetting singularity takes place at a finite distance from the obstacle as seen in the bottom left figure.

$$=\frac{\partial \rho}{\partial t}(\theta_{\min},1). \tag{43}$$

Defining the expressions $\rho_{\min}=\rho(\theta_{\min},1)$ and $\Delta\phi'_{\min}=\Delta\phi'(\theta_{\min},1)$ [$\phi'=\phi-\mathbf{v}\cdot\mathbf{r}$, see Eq. (10)] and using the continuity equation (9), $\rho_{\min}$ satisfies

$$\partial_t \rho_{\min} = -\rho_{\min}\Delta\phi'_{\min}, \tag{44}$$

which can be integrated as

$$\rho_{\min}(t) = \rho_{\min}(t_0)\exp\left[-\int_{t_0}^{t}\Delta\phi'_{\min}(u)du\right]. \tag{45}$$

Therefore, the minimum $\rho_{\min}$ decreases exponentially with time and can reach zero only when $\Delta\phi'_{\min}(t)\to\infty$.

Note that the dynamical equation for ϕ' is the Bernoulli equation

$$\partial_t\phi' = -\tfrac{1}{2}(\nabla\phi')^2+\tfrac{1}{2}v^2+1-\rho+\tfrac{1}{2}\xi^2\Delta\rho, \tag{46}$$

which, in the absence of the surface tension term, corresponds to the Euler equation known to present a finite-time singularity. To check such a behavior, we plot the logarithm of the density minimum and the velocity potential Laplacian. While the energy is conserved, the two latter quantities diverge at a finite time t^* as seen in Fig. 13. We have checked that this singularity is independent of the time-stepping schemes (leapfrog-Crank–Nicolson or implicit Euler schemes have been tested) and is not due to a lack of spatial or temporal resolutions.

VI. CONCLUSION

In summary, we have shown the existence of a saddle-node bifurcation for capillary-gravity flows around a cylindrical obstacle in the limit of small depth $H<\sqrt{3/2}\ell_c$. The saddle-node bifurcation of steady-state branches defines a critical speed above which no stationary solution exists. At subcritical speeds, the system can develop an instability if enough energy is provided for it to reach the unstable branch. The height of this nucleation barrier vanishes at the critical speed. This bifurcation is robust and thus is expected to survive even when effects neglected in the present study are taken into account, e.g., at finite but large enough Reynolds numbers. Note that at the critical speed the transition is continuous.

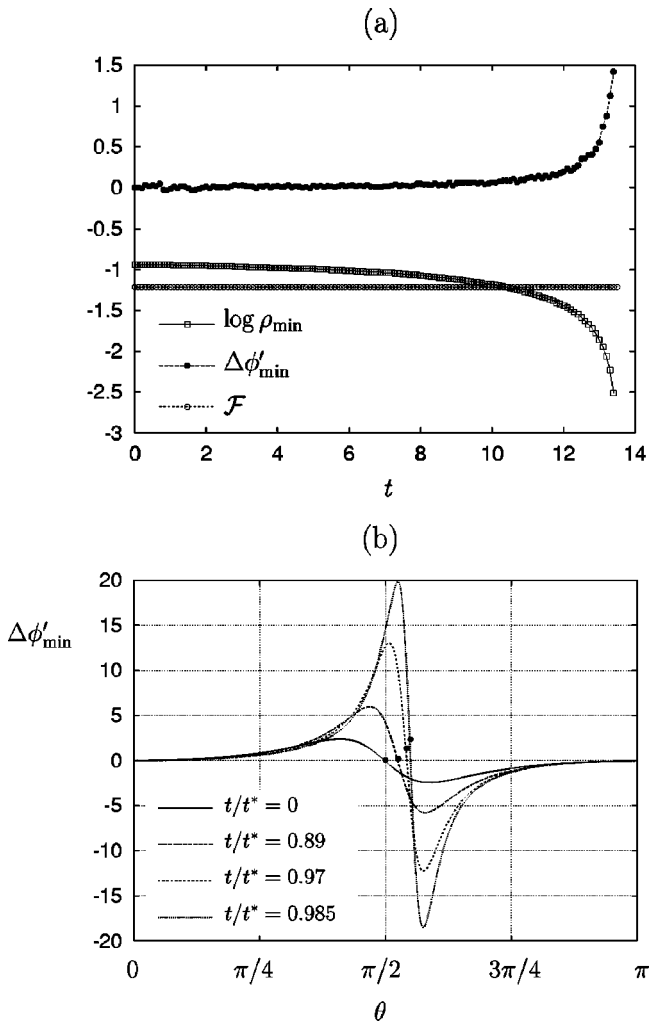

FIG. 13. Dewetting singularity for $\rho'_0=0$. (a) Top: Time evolution of the density minimum $\log \rho_{\min}$, the Laplacian of the velocity potential $\Delta\phi_{\min}$, and the energy $\mathcal{F}$ as indicated in the legend. The energy is numerically conserved until the singularity. (b) Bottom: the Laplacian of the velocity potential as a function of θ during time. Dots are the loci of the density minimum.

Furthermore, the nonlinear time evolution of this instability has been shown to lead to a finite-time dewetting singularity beyond which the shallow water description does not apply.

In the case of a two-dimensional nonlinear Schrödinger superflow past a disk, it has been shown that an unstable solution can emit a vortex pair corresponding to points where the density vanishes[11] for a small enough ratio $\xi_{\mathrm{NLS}}/D_{\mathrm{NLS}}$, where ξ_{NLS} is the so-called coherence length and D_{NLS} the diameter of the obstacle. The analog of the vortex pair formation in our present study is the dewetting singularity. However, when $\xi_{\mathrm{NLS}}/D_{\mathrm{NLS}}>15$, the emission of vortex pair is replaced by the emission of rarefation pulses, which are density depletion with nonzero density minimum.[17] In the case of our DSWE, it would be interesting to find if the equivalent of the rarefaction pulse emission (that is, the absence of vanishing density) exists in the limit of large ξ/D with appropriate boundary conditions (in ρ). This question is left for future study.

ACKNOWLEDGMENTS

This work was supported by ECOS-CONICYT under Program No. C01E08. Computations were performed at the Institut du Développement et des Ressources en Informatique Scientifique, Project No. 0283.

APPENDIX: SPECIALLY ADAPTED PSEUDOSPECTRAL METHOD

We have specifically developed a code that can accurately accommodate both large-r asymptotic behavior and thin boundary layers near the obstacle at $r=1$. It is based on a Chebychev decomposition using an adequate mapping. It allows us to consider a unique obstacle in contrast with periodic pseudospectral methods[11] which in fact model a network of obstacles.

A. Mapping for a unique obstacle

Using standard polar coordinates $\{\theta,r\}$, together with the relation

$$r(z)=z^{-1}, \tag{A1}$$

the domain $\{0\leqslant\theta<2\pi,-1\leqslant z\leqslant 1\}$ can be mapped into the physical domain $\{x,y\}$, with $x^2+y^2\geqslant 1$.

The basic mapping is

$$x=z^{-1}\cos\theta, \quad y=z^{-1}\sin\theta, \tag{A2}$$

and the inverse transformation reads

$$z=\pm\frac{1}{\sqrt{x^2+y^2}}, \quad \theta=\arctan(y/x)+\frac{\pi\mp\pi}{2}. \tag{A3}$$

Any generic real field $\psi(x,y)$ (ψ stands for the velocity potential ϕ or the density ρ) appearing in the encountered equations of motion is expressed in the $\{\theta,z\}$ domain as

$$\psi(\theta,z)=\psi[x(\theta,z),y(\theta,z)], \tag{A4}$$

with $x(\theta,z)$ and $y(\theta,z)$ defined in (A2).

As $x(\theta,z)=x(\theta+\pi,-z)$ and $y(\theta,z)=y(\theta+\pi,-z)$, the $\{x,y\}$ domain is mapped twice onto the $\{\theta,z\}$ domain. A mapped field must therefore satisfy

$$\psi(\theta,z)=\psi(\theta+\pi,-z). \tag{A5}$$

The equations of motion are expressed as partial differential equations in the $\{\theta,z\}$ domain by writing the differential operators ∇ and Δ in terms of θ and z derivatives that are polynomial in z, e.g., $\Delta\psi=z^2(\partial^2\psi/\partial\theta^2)+z^4(\partial^2\psi/\partial z^2)+z^3(\partial\psi/\partial z)$.

B. Spatial discretization

The field ψ is spatially discretized, in the (θ,z) domain, using a standard Chebychev–Fourier pseudospectral method,[21] based on the expansion

TABLE I. Azimuthal and radial resolutions used for computing the bifurcation diagram for different $\xi/\sqrt{2}D$ for the two types of boundary conditions.

$\xi/(\sqrt{2}D)$	$1/2$	$1/(2\sqrt{10})$	$1/20$	$1/40$	$1/80$
$N_\theta \times N_r$	64×32	64×32	64×64	128×128	128×256

$$\psi(\theta,z) = \sum_{n=1-N_\theta/2}^{N_\theta/2} \left\{ \sum_{p=0}^{N_r} \psi_{n,p} T_p(z) \right\} \exp in\theta, \tag{A6}$$

where $T_p(z)=\cos(p \arccos z)$ is the order-p Chebychev polynomial, and N_θ and N_r represent azimuthal and radial resolutions.

The pseudospectral method calls for using fast Fourier transforms to evaluate (A6) on the collocation points grid (θ_m, z_k) with

$$\theta_m = \frac{2\pi m}{N_\theta}, \quad 0 \leqslant m < N_\theta, \tag{A7}$$

$$z_k = \cos\frac{\pi k}{N_r}, \quad 0 \leqslant k \leqslant N_r. \tag{A8}$$

The relation $T_n(\cos x)=\cos nx$ reduces the Chebychev transform appearing in (A6) to a (fast) Fourier cosine transform. Thus, the evaluation of (A6) (and its inverse) only requires a time proportional to $N_\theta N_r \ln(N_\theta N_r)$. Computations of nonlinear terms are carried out on the grid representations, while θ and z derivatives are carried out on the Chebychev–Fourier representations.

The main virtue of mapping (A2) together with expansion (A6) is its ability to accurately accommodate both large-r asymptotic behavior and thin boundary layers near $r=1$. Indeed, on the one hand, (A6) is an expansion in product of polynomials in r^{-1} with functions $\cos n\theta$ and $\sin n\theta$, precisely the type of functions needed to capture large-r behavior (see Sec. IV A and Ref. 19). On the other hand, the accumulation of collocation points z_p [see Eq. (A8)] and the regularity of (A2) near $z=\pm1$ allows expansion (A6) to simultaneously resolve boundary layers at $r=1$ with thickness of order $1/N_r^2$ (see Ref. 21).

C. Spectral symmetries of the fields

As ψ is real, the coefficients $\psi_{n,p}$ in (A6) are complex conjugate,

$$\psi_{-n,p} = \overline{\psi}_{n,p}. \tag{A9}$$

They obey an additional relation, stemming from (A5). Setting $z=\cos(\theta')$, the fields must be invariant under the transformation $\theta \mapsto \theta+\pi$, $\theta' \mapsto \theta'+\pi$. In spectral space, this transformation reads $\psi_{n,p} \mapsto (-1)^n(-1)^p\psi_{n,p}$, implying

$$\psi_{n,p} = (-1)^{n+p}\psi_{n,p}. \tag{A10}$$

Thus the $\psi_{n,p}$ coefficients are nonzero only when (n,p) are jointly even or jointly odd. This relation, similar to that found in the Taylor–Green vortex,[22] is used to speed-up the evaluation of (A6) by a factor 2, using specially designed even-odd fast Fourier transforms.

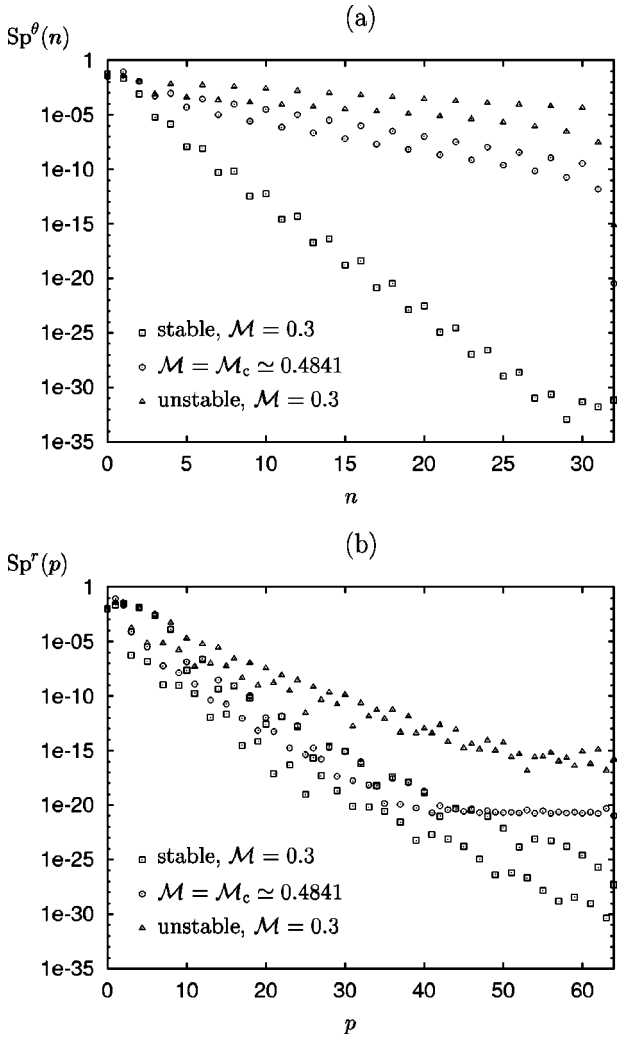

FIG. 14. Stationary solution spectra with $\xi/\sqrt{2}D=1/20$, $N_\theta\times N_r=64\times64$, and $\rho_0'=-5$: (a) θ spectra and (b) r spectra for a stable solution far from the bifurcation, for the solution at the bifurcation and for an unsteady solution. Spectral convergence is achieved for all stationary solutions.

Integrals of mapped fields are performed on the collocation points using the discrete formula

$$\int_\Omega r dr\, d\theta \psi(r,\theta) = -\frac{2\pi}{N_\theta}\frac{\pi}{N_r}\sum_{n=0}^{N_\theta-1}\sum_{p=0}^{N_r/2-1} \psi(\theta_m,z_k) \times\sqrt{1-z_p^2}\frac{dr}{dz}(z_p) r(z_p). \tag{A11}$$

D. Spectra

We define the r spectrum and θ spectrum of a field ψ spectrally represented by $\psi_{n,p}$ as the respective sequence of numbers,

$$\mathrm{Sp}^r(p) = \sum_{n=-(N_\theta/2)+1}^{N_\theta/2} |\psi_{n,p}|^2, \quad 0 \leqslant p \leqslant N_r, \tag{A12}$$

$$\mathrm{Sp}^{\theta}(n) = \sum_{p=0}^{N_r} |\psi_{n,p}|^2, \quad 0 \leqslant n \leqslant \frac{N_\theta}{2}. \tag{A13}$$

Only half of the θ spectrum is considered for the θ representation is complex conjugated.

E. Time steppings

1. Stationary States

We search for stationary solutions of the dynamic equations (8) and (9). Note that stationary solutions are those of the equivalent diffusive equations that read in the abbreviated form, by letting $\rho = 1 + \varrho$,

$$\frac{\partial \Psi}{\partial t} = L\Psi + W(\Psi), \tag{A14}$$

with

$$\Psi \equiv \begin{pmatrix} \phi \\ \varrho \end{pmatrix}, \quad L \equiv \begin{pmatrix} \Delta & 0 \\ 0 & \sigma\Delta \end{pmatrix}, \quad W \equiv \begin{pmatrix} \mathrm{NL}_\phi \\ \mathrm{NL}_\varrho \end{pmatrix}, \tag{A15}$$

and

$$\mathrm{NL}_\varrho(\phi, \varrho) = -\tfrac{1}{2}(\boldsymbol{\nabla}\phi)^2 - \varrho + \mathbf{v}\cdot\boldsymbol{\nabla}\phi, \tag{A16}$$

$$\mathrm{NL}_\phi(\phi, \varrho) = \varrho\Delta\phi + \boldsymbol{\nabla}\varrho\cdot\boldsymbol{\nabla}\phi - \mathbf{v}\cdot\boldsymbol{\nabla}\varrho. \tag{A17}$$

To integrate (A14) a mixed implicit-explicit first-order time-stepping scheme is used,

$$\Psi(t+\tau) = (\mathrm{Id} - \tau L)^{-1}(\mathrm{Id} + \tau W)\Psi(t), \tag{A18}$$

where Id is the identity operator and τ the time step.

The Helmholtz operator $(\mathrm{Id} - \tau L)$, block-diagonal with respect to Fourier modes, is easily inverted in the Fourier–Chebychev representation using the LU algorithm.[23]

As called for the τ method[21] the boundary conditions (12) and (13) are substituted to the Eq. (A14) for the highest Chebychev modes T_{N_r-1} and T_{N_r}. The operator $(\mathrm{Id} - \tau L)$ is thus modified before inversion.

This relaxation method can only reach stable stationary solutions of (A14). In order to also capture unstable stationary solutions[18] we use the Newton branch-following method detailed in Refs. 24, 10, and 11.

2. Branch-following Procedure

We search for fixed points of (A18), a condition strictly equivalent to the stationarity of (A14). Each Newton step requires solving a linear system for the decrement ψ to be substracted from Ψ,

$$[(\mathrm{Id} - \tau L)^{-1}(\mathrm{Id} + \tau DW) - \mathrm{Id}]\psi = [(\mathrm{Id} - \tau L)^{-1}(\mathrm{Id} + \tau W) - \mathrm{Id}]\Psi, \tag{A19}$$

where $DW(\Psi)$ is the Fréchet derivative, or Jacobian matrix, of W evaluated at Ψ. Equation (A19) is equivalent to

$$(\mathrm{Id} - \tau L)^{-1}\tau(L + DW)\psi = (\mathrm{Id} - rL)^{-1}\tau(L + W)\Psi. \tag{A20}$$

The role of τ is formally that of the time step in (A18), but in (A19) or (A20) its value can be taken to be arbitrarily large. For $\tau \to \infty$, (A20) becomes

$$L^{-1}(L + DW)\psi = L^{-1}(L + W)\Psi. \tag{A21}$$

In order to solve the linearized systems stemming from the Newton method, we use BiCGSTAB.[25] We vary τ empirically to optimize the preconditioning and convergence of BiCGSTAB. A few hundred BiCGSTAB iterations are usually required to solve the linear system.

3. Dynamics

We write (8) and (9) in the abbreviated form

$$\frac{\partial \Psi}{\partial t} = L'\Psi + W'(\Psi), \tag{A22}$$

where

$$\Psi \equiv \begin{pmatrix} \phi \\ \varrho \end{pmatrix}, \quad L' \equiv \begin{pmatrix} 0 & \sigma\Delta \\ -\Delta & 0 \end{pmatrix}, \quad W' \equiv \begin{pmatrix} \mathrm{NL}_\varrho \\ -\mathrm{NL}_\phi \end{pmatrix}, \tag{A23}$$

with NL_ϱ and NL_ϕ defined in Eqs. (A16) and (A17).

Equation (A22) is time stepped using either the leap-frog Cranck–Nicolson scheme

$$\Psi(t+\tau) = (1 - \tau L')^{-1}\{(1 + \tau L')\Psi(t-\tau) + 2\tau \mathrm{W}'[\Psi(t)]\} \tag{A24}$$

or the implicit Euler scheme

$$\Psi(t+\tau) = (1 - \tau L')^{-1}\{\Psi(t) + \tau \mathrm{W}'[\Psi(t)]\}. \tag{A25}$$

The boundary conditions (12) and (13) are imposed by modifying the operator $(1 - \tau L)^{-1}$, as done for the relaxation time-stepping algorithm (A14). The leap-frog Cranck–Nicolson scheme is initiated by an Euler time step and mixing steps[21] are performed periodically to avoid leap-frog instability.

F. Numerical convergence

Our numerical method based on Chebychev polynomial expansions allows to solve the boundary layer of order ξ by refining the collocation points near the boundary conditions. The smaller ξ is the larger the radial resolution N_r must be. Table I lists the resolutions used for computing the bifurcation diagram for each $\xi/\sqrt{2}D$. Spectral convergence is achieved for all stationary solutions as shown in Fig. 14.

[1] L. D. Landau and E. M. Lifshitz, *Fluid Mechanics*, 2nd ed. (Butterworth-Heinemann, Oxford, 1995).
[2] G. B. Whitham, *Linear and Nonlinear Waves* (Wiley-Interscience, New York, 1999).
[3] E. Raphaël and P.-G. de Gennes, "Capillary gravity waves caused by a moving disturbance: Wave resistance," Phys. Rev. E **53**, 3448 (1996).
[4] J. Browaeys, J.-C. Bacri, R. Perzynski, and M. Shliomis, "Capillary-gravity wave resistance in ordinary and magnetic fluids," Europhys. Lett. **53**, 209 (2001).
[5] T. Burghelea and V. Steinberg, "Onset of wave drag due to generation of capillary-gravity waves by a moving object," Phys. Rev. Lett. **86**, 2557 (2001).
[6] T. Burghelea and V. Steinberg, "Wave drag due to generation of capillary-gravity surfaces waves," Phys. Rev. E **66**, 051204 (2002).
[7] F. Chevy and E. Raphaël, "Capillary gravity waves: A fixed-depth analysis," Europhys. Lett. **61**, 796 (2003).
[8] Y. Pomeau and S. Rica, "Model of superflow with rotons," Phys. Rev. Lett. **71**, 247 (1993).
[9] T. Frisch, Y. Pomeau, and S. Rica, "Transition to dissipation in a model of superflow," Phys. Rev. Lett. **69**, 1644 (1992).

[10]C. Huepe and M. Brachet, "Solutions de nucléation tourbillonnaires dans un modèle d'écoulement superfluide," C. R. Acad. Sci., Ser. IIb: Mec., Phys., Chim., Astron. **325**, 195 (1997).
[11]C. Huepe and M. E. Brachet, "Scaling laws for vortical nucleation solutions in a model of superflow," Physica D **140**, 126 (2000).
[12]C. Raman, M. Köhl, R. Onofrio, D. S. Durfee, C. E. Kuklewicz, Z. Hadzibabic, and W. Ketterle, "Evidence for a critical velocity in a Bose-Einstein condensed gas," Phys. Rev. Lett. **83**, 2502 (1999).
[13]E. P. Gross, "Structure of a quantized vortex in boson systems," Nuovo Cimento **20**, 454 (1961).
[14]V. L. Ginzburg and L. P. Pitaevskii, "On the theory of superfluidity," Sov. Phys. JETP **7**, 858 (1958).
[15]F. Dalfovo, S. Giorgini, L. P. Pitaevskii, and S. Stringari, "Theory of Bose-Einstein condensation in trapped gases," Rev. Mod. Phys. **71**, 463 (1999).
[16]É. Guyon, J.-P. Hulin, and L. Petit, *Hydrodynamique Physique*, 2nd ed. (EDP Sciences, Les Ulis, 2001).
[17]C.-T. Pham, "Stabilité et dynamique d'écoulements de fluides parfaits barotropes autour d'un obstacle en présence de dispersion" Ph.D. thesis, Université Paris 6, 2003.
[18]R. Seydel, *From Equilibrium to Chaos: Practical Bifurcation and Stability Analysis* (Elsevier, New York, 1988).
[19]S. Rica, "A remark on the critical speed for vortex nucleation in the nonlinear Schrödinger equation," Physica D **148**, 221 (2001).
[20]T. Podgorski, J.-M. Flesselles, and L. Limat, "Dry arches within flowing films," Phys. Fluids **11**, 845 (1999).
[21]D. Gottlieb and S. A. Orszag, *Numerical Analysis of Spectral Methods* (SIAM, Philadelphia, 1977).
[22]C. Nore, M. Abid, and M. Brachet, "Decaying Kolmogorov turbulence in a model of superflow," Phys. Fluids **9**, 2644 (1997).
[23]W. H. Press, S. A. Teukolsky, W. T. Vetterling, and B. P. Flannery, *Numerical Recipes*, 2nd ed. (Cambridge University Press, Cambridge, 1992), Chap. 9, p. 372.
[24]L. S. Tuckerman and D. Barkley, "Bifurcation analysis for time-steppers," *Numerical Methods for Bifurcation Problems and Large-Scale Dynamical Systems*, edited by E. Doedel and L. S. Tuckerman (Springer, New York, 2000), Vol. 7, pp. 452–466.
[25]H. A. Van Der Vorst, "BI-CGSTAB: A fast and smoothly converging variant of BI-CG for the solution of nonsymmetric linear systems," SIAM (Soc. Ind. Appl. Math.) J. Sci. Stat. Comput. **13**, 631 (1992).